Study on adsorption of Direct Red 23 by biochar derived from co-pyrolysis of sewage sludge and rice husk waste: optimization, isotherm, kinetic, thermodynamic and mechanisms

Si Chen[a,b], Teng Wang[a,b], Chang Chen[c], Jingxin Liu[a,b], Meng Mei[a,b], Junpu Xie[a,b],*, Jinping Li[a,b],*

[a]School of Environmental Engineering, Wuhan Textile University, Wuhan 430073, China
[b]Engineering Research Centre for Clean Production of Textile Dyeing and Printing, Ministry of Education, Wuhan Textile University, Wuhan 430073, China, Tel. +86 13720232678; Fax: +86- 027-59367338; emails: 1807705553@qq.com (J. Xie), wtu2019098@163.com (J. Li), whuchensi8683@163.com (S. Chen), 459010939@qq.com (T. Wang), 1702981502@qq.com (J. Liu), 2427327023@qq.com (M. Mei)
[c]Hubei Environmental Remediation Material Engineering Technology Research Center, Wuhan University, Wuhan 430074, China, email: 2387773648@qq.com

ABSTRACT

Co-pyrolysis of sewage sludge and rice husk is a promising sludge treatment and resource utilization method. In this work, the pyrolysis conditions of sewage sludge and rice husk were optimized to obtain the optimal biochar (OB) with the highest capacity for Direct Red 23 (DR23). Adsorption isotherm, kinetics, thermodynamics and mechanism of DR23 onto OB and modified OB by oxalic acid (OAOB) were also investigated. Results revealed that the pyrolysis temperature (651.444°C), heating rate (10°C/min), and residence time (4.683 h) were the best preparation conditions of biochar for adsorption of DR23; OB and OAOB both have high adsorption capacities towards DR23: 313.48 and 336.70 mg/g, respectively; The adsorption data fitted the Freundlich, Langmuir and Temkin models well, the adsorption kinetics obeyed pseudo-second-order model, and the sorption was spontaneous and endothermic; Adsorption mechanisms of DR23 onto OB and OAOB were mainly chemisorptions and contained functional group interaction between –OH, –COOH on surface of OB with DR23, and between –OH, –COOH, –COOR on surface of OAOB with DR23, π–π stacking interaction, electrostatic interaction and surface participation. This work was beneficial for the resource utilization of sludge and rice husk, and provided targeted adsorbent for the removal of DR23 from wastewater.

Keywords: Co-pyrolysis; Optimization; Isotherm; Kinetics; Thermodynamics; Mechanism

1. Introduction

Sewage sludge is a by-product from wastewater treatment process, more than 60 million tons sewage sludge (moisture of 80%) is produced annually in China [1]. Sludge contains various heavy metals, organic toxic substances and pathogens, the large-scale direct disposal will pollute the soil and water. Thus posing a risk to the health of animals and human beings. Hence sludge treatment has attracted much attention [2]. Currently, the commonly used methods for sludge treatment are landfill, soil utilization, incineration, anaerobic digestion, and composting [3]. By these ways, the second pollution problems may often be caused. The pyrolysis of sludge is one of the resource utilizations,

* Corresponding authors.

and the pyrolysis products (biochar) have been applied as an absorbent for the removal of heavy metals and toxic organic compounds from wastewater [4–7], which not only solves the problem of sludge massive accumulation but also provides an economical and environmental friendly adsorbent for pollution treatment.

DR23 is one of the azo dyes, it is widely used in textile, print, paper and cosmetics industry [8], the azo groups in the DR23 are carcinogenic, mutagenic, and teratogenic to humans and aquatic organisms, and it is not quickly biodegraded. Hence the wastewater polluted by azo dyes must be treated before discharging into the water [9]. At present, the main methods for treatment of dye wastewater are biological treatment, membrane treatment, chemical oxidation, photo-degradation, electrocoagulation and adsorption treatment [10,11]. Adsorption method has the advantages of low cost, environmental friendly, simple operation and sensitive to contamination. Hence it is considered to be a better method to treat dye wastewater. Activated carbon, as the traditional adsorbent, is expensive and the preparation process is complicated [12]. It is very urgent to explore some new excellent adsorbents for the adsorption of dye-contaminated wastewater [13]. In recent studies, there have been some materials used in adsorbing dyes from the wastewater, such as clay and modified clay [14], agricultural solid waste [11,15], chitosan composites [16], graphene [17], carbon nanotubes [18], etc., which are effective and economical for removal of dye from wastewater.

Biochar is porous, environment-friendly, rich in mineral elements, and it also has a large specific area [19]. It is prepared by pyrolysis of animal manure, waste biomass, sludge, etc. under limited or no oxygen conditions [14,20]. The surface of biochar contains rich oxygen-containing functional groups, such as carboxylate (–COO−) groups, carbonyl (–C=O), and hydroxyl (–OH), which can interact with the heavy metals and surface functional groups of organic contaminations [21,22]. Several papers have used the biochar to remove pesticides, antibiotics, and dyes from wastewater [23–30]. However, sludge-based biochar has been used by many researchers for adsorption of DR23 from aqueous solutions. No attempt has been carried out till now to use the sludge-based biochar prepared at optimal conditions for DR23 adsorption. Rice husk is

one of low-cost and environment-friendly biomass, and nearly 30 million tons of rice husk are produced every year in mainland China. A large number of studies had verified that the biomass can be beneficial to the formation of pore structure during pyrolysis and then improve the adsorption capacity of sludge biochar [31,32]. In our previous study, when the content of rice was 30%, the sludge-rice husk biochar had the best adsorption properties [31]. Therefore, in this study, in order to prepare a highly efficient, economic, environmental friendly adsorbent for removal of the harmful dye DR23, the waste of sludge and rice husk (with ratio of 7:3), which their massive accumulation has serious environmental problems, have been selected as raw materials for preparation of biochar. The preparation process was optimized by the RSM software, obtaining the optimal adsorptive biochar for DR23. And for further improving adsorption capacity, the optimized sludge biochar was modified by oxide acid. The adsorption isotherm, kinetics, thermodynamics and mechanism of DR23 onto this novel adsorbent were also discussed. The study on adsorption of DR23 by co-pyrolysis products of sludge and rice husk in mechanism level solved the resource utilization of sludge and rice husk, and provided targeted adsorbent for the removal of DR23 from wastewater.

2. Materials and methods

2.1. Materials

DR23 (C.I. 29160) has a molecular weight of 790.69 g/mol, and the maximum wavelength of 502 nm. DR23 usually converts in the aqueous solutions into negatively charged ions and Sodium cations. The chemical structure of DR23 is shown in Fig. 1.

The source and pretreatment of sludge, rice husk and DR23 sample are consistent with our previous article [32].

2.2. Preparation of biochar

According to our previous studies [31], when the rice husk content was 30%, the biochar had the best adsorption performance. So, 30% rice husk and 70% sewage sludge mixture were used as the raw materials. The method of
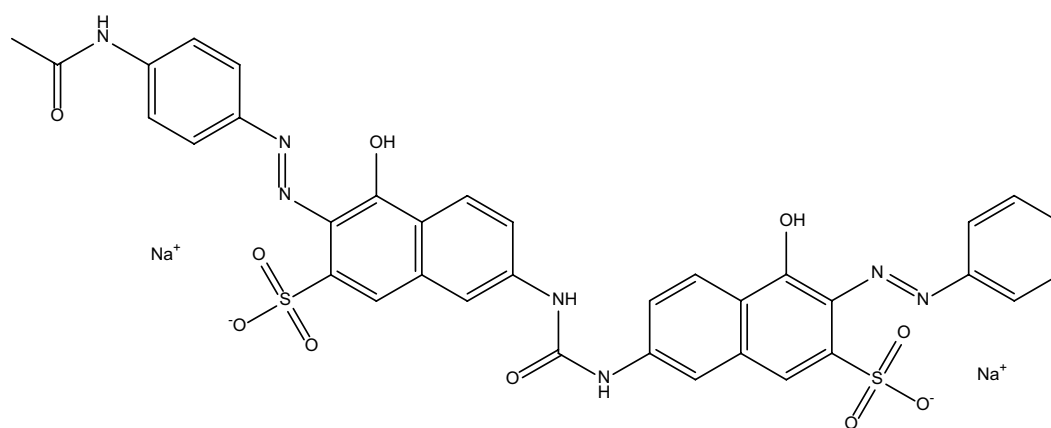

Fig. 1. Chemical structure of DR23.

blend is the same as the method used in our previous study [32]. The sieved mixture powder was pyrolyzed under argon condition by a tubular furnace, the temperature was set from 20°C to the final pyrolysis temperature, at a specified heating rate and maintained for a specified time. The prepared biochar was stored in a closed container for the subsequent experiments.

The optimal biochar called OB was chosen to adsorb DR23, and it was also modified by oxalic acid for improving adsorption capacity. The modifying process is as follows: 1 g OB was added to 50 mL of 1 mol/L oxalic acid solution, and then the suspension was kept in a shaking water bath for 2 h at room temperature with the rotation rate of 150 rpm, and then dried in an oven for 24 h at 60°C. The temperature was then increased to 120°C and maintained for 3 h. The oxalic acid modified OB called OAOB was collected through centrifuging and rinsed repeatedly with deionized water. Finally, the solid then was oven-dried at 60°C for 24 h, crushed and stored in a closed container for subsequent experiments.

2.3. Experimental design and adsorption studies

The statistical software Design-Expert trial version 10 was applied to design the experiment, and the preparation conditions of sludge biochar were optimized by the response surface methodology (RSM). The temperature (°C), heating rate (°C/min) and residence time (h) were chosen as the preparation factors, and the adsorption capacity of the DR23 was selected as the response. Table 1 shows the ranges and the levels of the factors investigated in this study. The total number of experiments was 17 and all of them are listed in Table 2. The goal was to get the maximum adsorption capacity of DR23.

It was assumed that the relationship between response and the three independent factors follows a quadratic equation, as given by Eq. (1):

$$Y = b_0 + b_1 X_1 + b_2 X_2 + b_3 X_3 + b_{12} X_1 X_2 + b_{13} X_1 X_3 + b_{23} X_2 X_3 + b_{11} X_{11}^2 + b_{22} X_{22}^2 + b_{33} X_{33}^2 \tag{1}$$

where Y is the response variable (adsorption capacity of DR23 onto sludge-rice husk biochar), b_0 represents a content, b_1, b_2 and b_3; b_{12}, b_{13} and b_{23}; b_{11}, b_{22} and b_{33} are all the coefficients.

The experiments of DR23 adsorption onto sludge-rice husk biochar prepared at different conditions were conducted in a shaking water bath at 180 rpm for 24 h as follows: 0.10 g of each biochar was added into 50 mL of 200 mg/L DR23 solution at 25°C, and pH 6–7, the biochars were removed by filtering after adsorption process, and then the concentration of residual DR23 was determined.

Table 1
Ranges and levels of the factors in the optimization experiment using the Box–Behnken design

Independent variable	Symbol	Coded variable level	
		Low (–1)	High (1)
Temperature (°C)	X_1	300	700
Heating rate (°C/min)	X_2	2.5	10
Residence time (h)	X_3	2	6

Table 2
Experimental design matrix for biochar preparation and response

Standard order	Factors in uncoded levels			Response Y
	X_1: temperature (°C)	X_2: heating rate (°C/min)	X_3: residence time (h)	Adsorption capacity (mg/g)
1	0	0	0	88.71
2	0	0	0	87.24
3	–1	0	1	44.655
4	0	0	0	87.35
5	1	1	0	99.73
6	–1	1	0	53.31
7	0	1	1	93.38
8	0	1	–1	86.73
9	0	–1	1	86.43
10	1	0	–1	94.26
11	0	0	0	85.51
12	1	0	1	95.04
13	0	0	0	88.53
14	1	–1	0	100
15	–1	0	–1	37.96
16	–1	–1	0	51.17
17	0	–1	–1	87.24

2.4. Instrument analyses

Brunauer–Emmett–Teller (BET) method, Element analyzer, inductively coupled plasma optical emission spectrometry (ICP-OES), X-ray diffraction (XRD), X-ray photo-electronic spectroscopy (XPS) and the Fourier transform infrared (FTIR) spectroscopy were used to detect the physical and chemical properties. The zeta potentials of OB and OAOB before and after adsorption of DR23 at different pH were measured to investigate the changes of surface potential as the increasing of pH value. The instrument models and zeta potential testing process referred our previous work [32].

2.5. DR23 adsorption batch experiments

The adsorption batch experiments were conducted in the shaking water bath, the experimental conditions and runs of pH influence, adsorption isotherm, kinetics, and thermodynamics are shown in Table 3. The pH was adjusted with HCl (0.1 mol/L) and NaOH (0.1 mol/L) and the pH meter was used to measure the pH values. After adsorption, the solution was collected by syringe with 0.45 um filter membrane, and the UV-vis Spectro Meter was applied to measure the concentration of residual DR23. Every adsorption experiment was repeated and only the average was used as the analytical value. Using Eq. (2) to calculate the adsorption capacities of OB and OAOB for DR23:

$$q_t = \frac{V(C_0 - C_t)}{m} \tag{2}$$

where q_t (mg/g) is the adsorption capacity of DR23 at time t, V (L) is the volume of the DR23 solution, C_0 (mg/L) and C_t (mg/L) are the concentration of the DR23 solution at initial and time t, m (g) is the weight of the biochar.

3. Results and discussion

3.1. Optimization of pyrolysis conditions and statistical analysis

The Box–Behnken design was applied to evaluate the experimental results and obtain the approximate functions for the adsorption capacity of DR23 (dependent variable Y). From the fitting of the data, fitting polynomial Eq. (3) is given as follows:

$$Y = 87.47 + 25.24X_1 + 1.04X_2 + 1.66X_3 - 0.60X_1X_2 - 1.48X_1X_3 \\ + 1.86X_2X_3 - 15.94X_1^2 + 4.53X_2^2 - 3.55X_3^2 \tag{3}$$

where X_1, X_2, and X_3 represented the coded values of the three factors: pyrolysis temperature, heating rate and residence time, respectively.

The variance regression model analysis of the adsorption capacity of DR23 is given in Table 4. The F value in the model was 191.09, and the value of "Prob. > F" was <0.0001, revealing the variance regression model was significant. What's more, the "lack of fit F-value" was 3.91, compared with the pure error, it was not significant, which proved again that the model is good. The R^2 of fitting experimental values and predicted values was 0.9959 as shown in Fig. 2, illustrating the model could well represent the composite condition behavior of DR23 adsorption capacity. The terms, which value of "Prob. > F" less than 0.05000 in the model, are considered to be significant, so the significant terms in this case were X_1, X_3, X_{12}, X_{22}, and X_{32}.

As shown in Table 5, the goal of the optimization was to determine certain pyrolysis temperature, heating rate, and residence time, under these conditions the sludge biochar was prepared and it had the highest adsorption capacity towards DR23. Optimized by the RSM, the target values of the three factors were $X_1 = 0.755$, $X_2 = 1$, and $X_3 = 0.342$. Accordingly, the pyrolysis temperature, heating rate, and residence time were 651.444°C, 10°C/min, and 4.683 h, respectively.

Fig. 3 shows the three-dimensional response surfaces of the three factors generated using Design-Expert software. When two of the factors were discussed, the third factor was kept at the zero level. Fig. 3a shows that the adsorption capacity increased as the temperature increasing at the range of 300°C–651.4°C, under the combined effect of pyrolysis temperature (X_1) and heating rate (X_2), while, when temperature was more than 651.4°C, higher temperature had a negative effect. The heating rate had negative effect on adsorption capacity at the initial stage, and became positive effect at the next stage, so the response surfaces had a depression in the middle. The combined effect of pyrolysis temperature (factor X_1) and residence time (factor X_3) was significant to the adsorption capacity of DR23 onto the biochar prepared at the heating rate 6.25°C/min (Fig. 3b). Fig. 3c shows that the combined effect of heating rate (X_2), residence time (X_3) is not obviously at the temperature 500°C. The results indicate that the pyrolysis temperature was the dominant determinant.

Table 3
Runs and conditions of the DR23 adsorption onto OB and OAOB

Experimental item	Solution concentrations of dyes (mg/L)	Sampling time (min)	Temperature (°C)	pH
Adsorption isotherms	100–800 (100, 200, 300, 400, 500, 600, 700, 800)	1,440	25	6–7
Adsorption kinetics	400	5–1,440 (5, 10, 30, 60, 120, 240, 720, 1,440)	25	6–7
Adsorption thermodynamics	100–800 (100, 200, 300, 400, 500, 600, 700, 800)	1,440	25, 35, 45	6–7
Effects of pH	400	1,440	25	3, 5, 7, 9, 11

Table 4
Analysis of the variance regression model for the adsorption capacity of DR23

| Source	Sum of squares	df	Mean square	F value	p-value Prob. > F
Model	6,353.54	9	705.95	191.09	<0.0001
X_1	5,097.22	1	5,097.22	1,379.77	<0.0001
X_2	8.63	1	8.63	2.34	0.1702
X_3	22.16	1	22.16	6.00	0.0442
X_1X_2	1.45	1	1.45	0.39	0.5506
X_1X_3	8.75	1	8.75	2.37	0.1678
X_2X_3	13.91	1	13.91	3.77	0.0934
X_1^2	1,069.94	1	1,069.94	289.62	<0.0001
X_2^2	86.23	1	86.23	23.34	0.0019
X_3^2	53.01	1	53.01	14.35	0.0068
Residual	25.86	7	3.69		
Lack of fit	19.29	3	6.43	3.91	0.1102
Pure error	6.57	4	1.64		
Cor. rotal	6,379.40	16			
Std. dev.	1.92	R^2		0.9959	
Mean	80.43	Adj. R^2		0.9907	
C.V. %	2.39	Pred. R^2		0.9500	
PRESS	318.90	Adeq. precision		42.151	
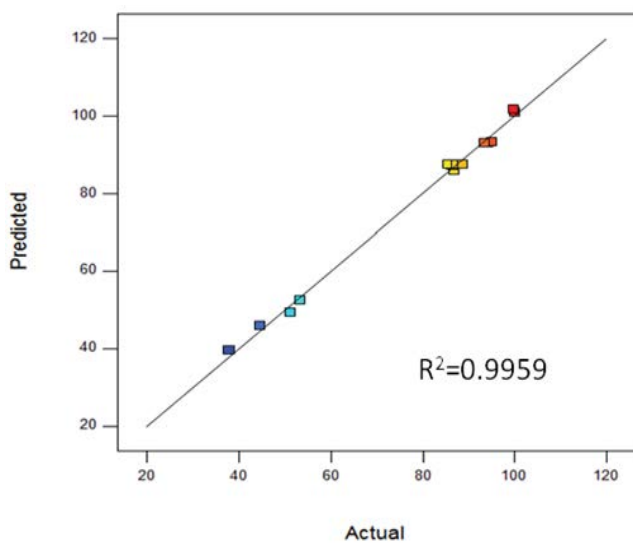
Fig. 2. Relationship between the predicted and actual values for the adsorption capacity of DR23.

3.2. Characterization of the adsorbent

3.2.1. Element contents and physical properties

Table 6 presents the part of the element contents and the typical physical properties correlative to the adsorption capacity of the OB and OAOB. The structure of the biochar has a great influence on its adsorption performance, larger BET surface area and total pore volume cause larger physical adsorption ability [2], after modified with oxalic acid, the BET surface area, total pore volume both increased, indicating OAOB had stronger physical adsorption of DR23 than OB. The pore diameter also plays a significant role in the physical adsorption performance of biochar, the adsorption theory implies that the adsorbent presents best adsorption property, when the pore size of adsorbent is 1.7–3 times larger than the molecular size of adsorbate, the adsorbent performs good adsorption property, when it is 3–6 times larger or even more, it can be regenerated well [2]. The molecular size of the DR23 was 3.20 nm long, 1.32 nm wide, 0.92 nm high, which were calculated using the Chem3D software, the calculating process as follows: the 3D structures of

Table 5
Criteria for the factors and the response for the optimization

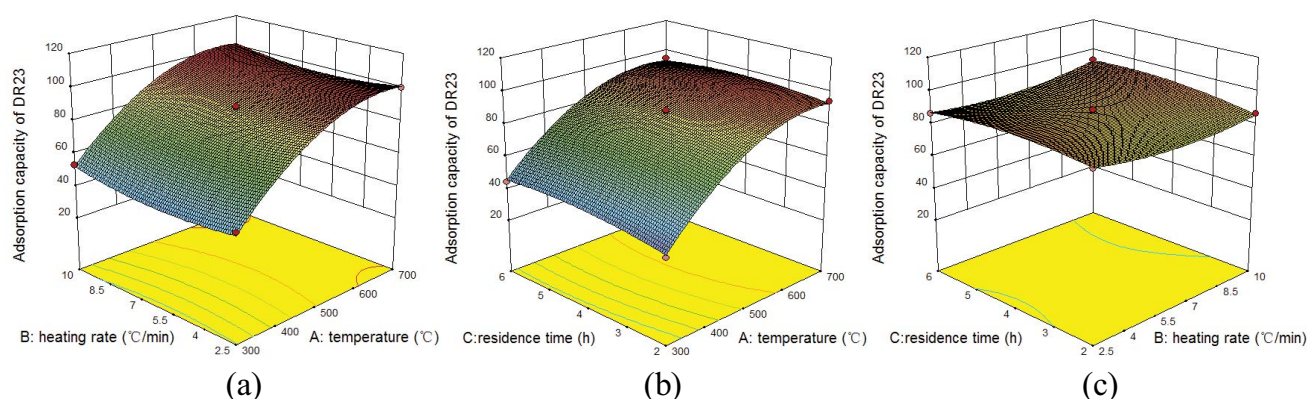| Variable	Goal	Lower limit	Upper limit	Importance
X_1, temperature (°C)	In range	300	700	3
X_2, heating rate (°C/min)	In range	2.5	10	3
X_3, residence time (h)	In range	2	6	3
Adsorption capacity of DR23	Maximum			3

Fig. 3. Response surface plots: (a) heating rate and temperature, (b) residence time and temperature, and (c) residence time and heating rate.

Table 6
Element contents and physical properties of the OB and OAOB

	Element contents (%)									
Biochar	C	H	N	S	K	Na	Mg	Al	Fe	Ca
OB	8.20	0.377	0.67	0.612	1.965	0.669	1.394	11.432	6.099	2.677
OAOB	10.87	1.207	0.61	0.521	2.081	1.016	0.544	5.0428	5.595	2.280

	Physical characterization		
Biochar	BET surface area (m²/g)	Total pore volume (cm³/g)	Average pore diameter (nm)
OB	113.527	0.134	4.722
OAOB	161.555	0.205	5.072

the molecules were drawn in chem3D software, and then the molecular structures were optimized with the lowest energy, the distance between the two atoms with the maximum distance was measured as the size of the molecule by selecting the *X-Y*, *X-Z*, *Y-Z* angle of view [33]. OB had the average pore diameter of 4.7217 nm, and OAOB had that of 5.0722 nm, which were favorable for the adsorption of DR23, and the average pore diameter of OAOB larger than that of OB, the OAOB may present better adsorption property of DR23 than OB. After modifying, the content of carbon increased, suggesting the oxalic acid reacted with molecules of OB, and the carbon in oxalic acid was introduced into OB, offering new adsorption sites for the molecule of DR23. The contents of Mg, Al, Fe, Ca all decreased, because of the dissolution of minerals in OB by oxalic acid, which made the number of pores on surface of OB increased, thereby the total pore volume and specific surface area increased.

3.2.2. XRD spectra of biochar

The XRD spectra of the OB and OAOB in the range of 3°–80° were detected to obtain their chemical composition as shown in Fig. 4. The spectra showed that the surface of OB was mainly composed of C substrate and SiO_2, after modification by OA, the new peaks appeared, they were ascribed to $CaC_2O_4 \cdot H_2O$. It was because that the OA interacted with the calcium in the OB, and it might offer new sites for the adsorption of DR23.
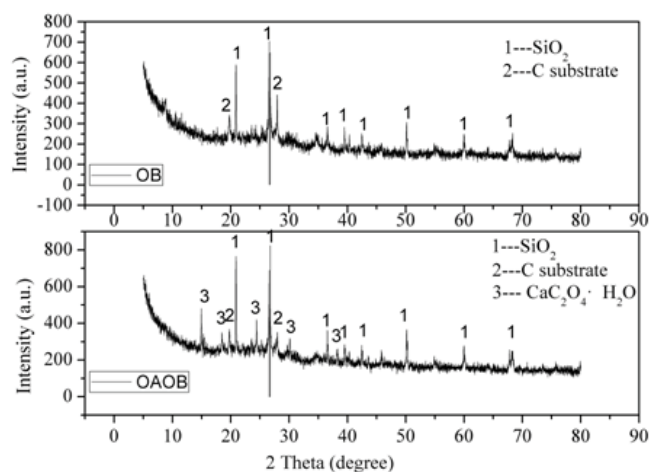

Fig. 4. XRD spectra of OB and OAOB.

3.3. Effect of adsorption condition

3.3.1. Effect of pH on adsorption

Fig. 5a is the curve of pH effect on adsorption capacity, the adsorption capacity of DR23 onto OB and OAOB both decreased as the pH increased, because when the pH value was 3, both the OB and OAOB carried positive charges on the surface, while the DR23 molecule was negatively charged,

the electrostatic attraction between biochar and DR23 molecule caused the highest adsorption capacity of OB and OAOB at this pH value. As the pH increases, the surface potential of OB and OAOB became negative, electrostatic repulsion between biochar and DR23 appeared, and the larger the pH value was, there were more negative charges on the surface of OB and OAOB, leading gradual decrease of adsorption capacity. The result indicated that lower pH value was more propitious to the DR23 sorption, and the electrostatic interaction accounted for a large proportion in the adsorption process.

3.3.2. Effect of contact time on adsorption

As Fig. 5b shows, at the beginning time, the adsorption capacity of DR23 onto OB and OAOB both increased rapidly, then, decreased gradually, and finally achieved stability. Before 598 min, the adsorption capacity of DR23 onto OB was higher than that onto OAOB. And because of having more adsorption sites of OAOB, the adsorption capacity of DR23 onto OAOB exceeded that of OB after 598 min. The adsorption of DR23 onto OB and OAOB both reached equilibrium at nearly 720 min.

3.3.3. Effect of initial concentration on adsorption

As shown in Fig. 5c, the adsorption capacity of DR23 onto OB and OAOB both increased as the initial concentration increased. When the initial concentration was lower than 200 mg/L, the adsorption capacity of DR23 onto OB was slightly higher than that onto OAOB, but at the initial concentration of 260 mg/L, the adsorption capacity of DR23 onto OAOB began gradually higher than that onto OB, indicating that the low initial concentration was beneficial for the adsorption of DR23 onto OB. The increased initial concentration led adsorption of DR23 to saturation and the adsorption capacity tended to equilibrium, while the adsorption sites of OAOB were more than those of OB, and it can carry more DR23 molecules, leading to the higher adsorption capacity of DR23 onto OAOB at high initial concentration.

3.4. Comparison of biochar characteristics before and after adsorption

3.4.1. FTIR characteristics of biochar before and after adsorption

FTIR spectroscopy was used to detect the surface functional group vibration changes of the adsorbent before and after modifying/adsorption by monitoring the peak changes in position and intensity. The FTIR spectra of the OB, OAOB, OB-DR23, OAOB-DR23 are presented in Fig. 6, and the attribution of functional groups are listed in Table 7. The peak at 1,036 cm^{-1} in OB changed to 1,081 cm^{-1} in OAOB (C-OH stretching), the new peaks at 1,314; 1,420 cm^{-1} (calcium oxalate hydrates) appeared in OAOB [34], showing that the oxalic acid interacted with the calcium on the surface of OB, the result was consistent with the XRD result. The peak at around 1,615 cm^{-1} of OAOB became much sharper than that of OB, and divided into two peaks at 1,615 and 1,666 cm^{-1} (C=O stretching in carboxylic, –COOR antisymmetric stretching), showing a large number of –COOH and –COOR

emerged after modification of OA, the peak at 3,431 cm^{-1} (O–H stretching) in OB changed into two peaks at 3,342 and 3,423 cm^{-1} in OAOB, showing that O–H interacted with the OA [35]. According to the above analysis, the modification mechanism of OA could be expressed as follows:

When comparing the FTIR spectra of OB and OB-DR23, OAOB and OAOB-DR23, it could be found that, after adsorption of DR23, new peaks appeared at around 1,385; 1,492; and 1,535 cm^{-1} (C–NO$_2$ symmetric stretching, CH$_3$ asymmetric bending, and C–N stretching in DR23), indicating that numerous DR23 molecules were attached on the OB and OAOB surface after adsorption of DR23. Peaks position of OB shifted at around 1,618 and 3,431 cm^{-1} (they were ascribed to C=O stretching in carboxylic, and O–H stretching) after adsorption of DR23, showing that DR23 interacted with O–H and –COOH on the surface of OB [36,37]. The peaks position of OAOB shifted at around 1,615; 1,666; 3,342 cm^{-1} (C=O stretching in carboxylic, COO$^-$ antisymmetric stretching, stretching, O–H stretching), indicating that DR23 also interacted with O–H, –COOH, and esters groups (–COOR) on the surface of OAOB [38].

3.4.2. XPS characteristics before and after adsorption

The XPS spectra of OB and OAOB before and after adsorption of DR23 were shown in Fig. 7, the corresponding data are shown in Table 8. Figs. 7a and b show that the adsorption peaks of OB and OAOB appeared at around 284.6, 399.8 and 531.8 eV, which corresponded to C 1s, N 1s and O 1s, respectively. The analysis of FTIR indicated that the carbon atom in OB and OAOB has the most binding form of chemical bonds, and the photoelectron peaks of C 1 s of OB and OAOB were both obvious; therefore, the binding energy changes of each chemical bond of C 1s and the relative contributions were used to analyze the change of functional groups before and after modification/adsorption. As shown in Figs. 7c and d, the adsorption peak at 284.6 eV attributed to C 1s, according to the previous reports about the XPS [39,40], the C 1s photoelectron peak was decomposed into six peaks at 284.3, 284.8, 285.3, 286.4, 288.9 and 290.8 eV, which denoted C1a, C1b, C2a, C2b, C2c and C3, respectively. Two peaks C1a and C2a correspond to non-functionalized carbon sp^2 and sp^3 atoms. Three other peaks at 285.3, 286.4 and 288.9 eV were assigned to carbon atoms bound with oxygen atoms, representing C–O–, C=O and COO– groups. As Table 7 shows, the total nitrogen content was very low, there was no need to describe. The C3 attributed to π–π shake-up of the sp^2-hybridized carbon atoms conclude the model applied in the peak fitting procedure, which was not obvious in the XPS spectra of OB and OAOB in this study. As shown in Figs. 7c, d and Table 8, the adsorption peaks of C2a, C2b, C2c corresponding to C–O, C=O and COO– in OB and OAOB all shifted obviously, which indicated that the C–O, C=O– and COO– in OB and OAOB both interacted with
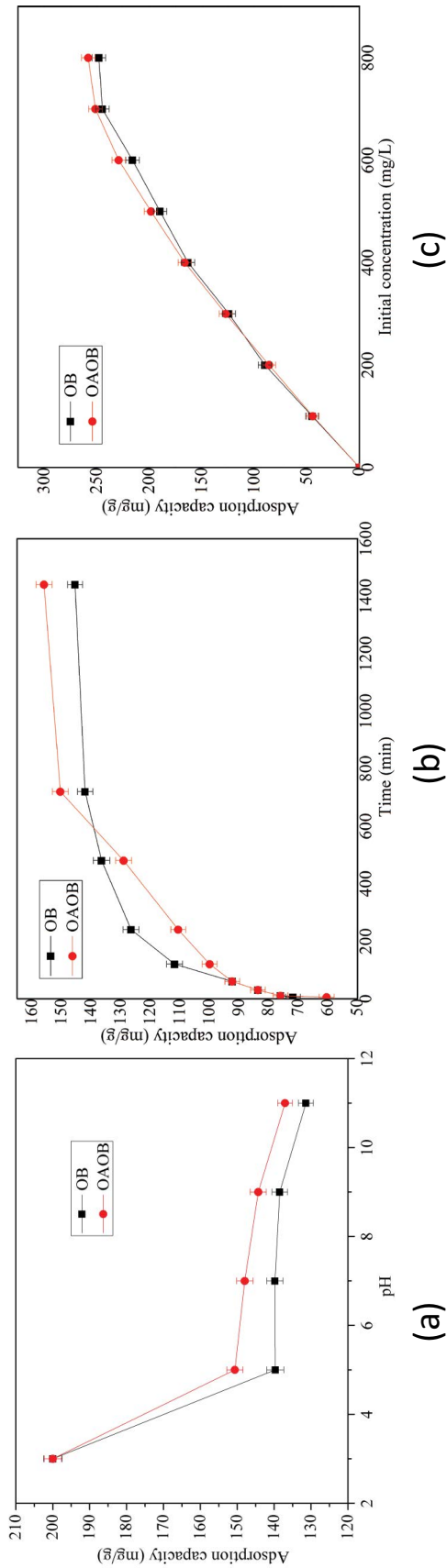
Fig. 5. Effect of adsorption condition on the adsorption of DR23, (a) pH effect, (b) contact time effect, and (c) initial concentration effect.
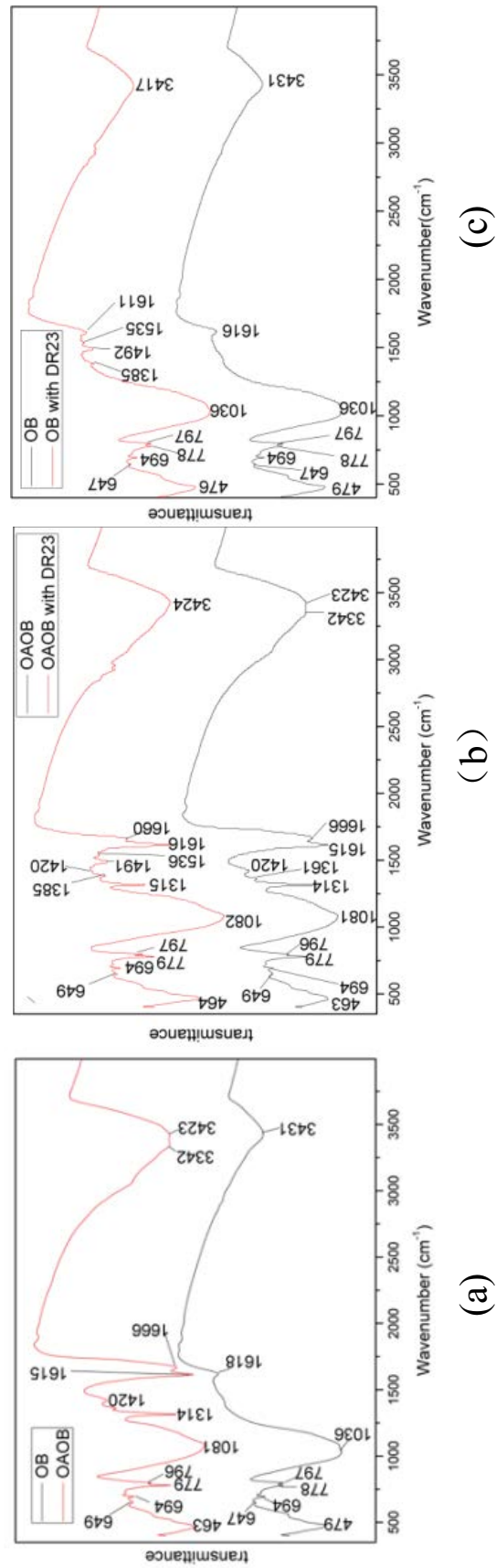

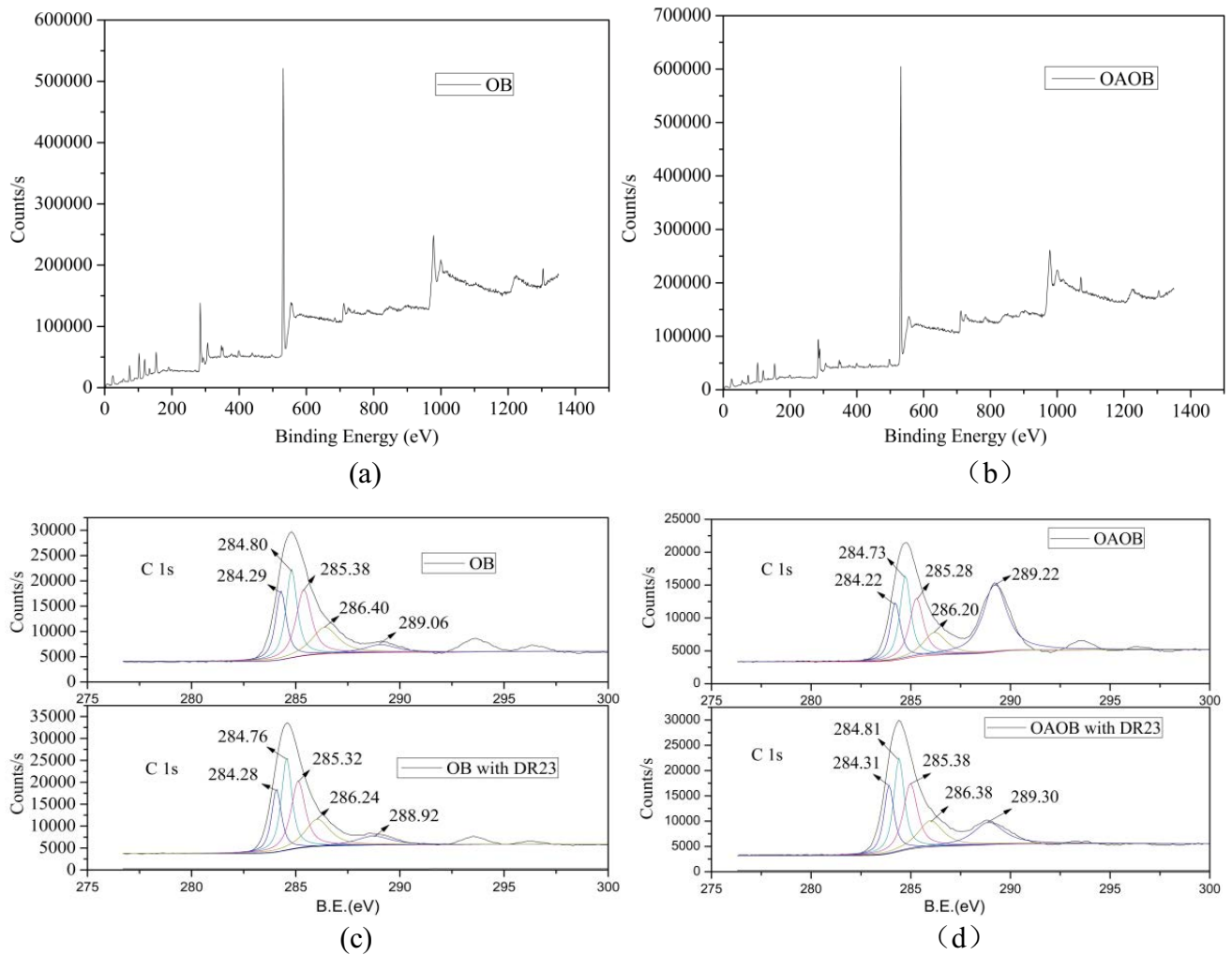Fig. 6. FTIR spectra of the two biochar before and after the adsorption of DR23.

Fig. 7. XPS spectra of OB and OAOB before and after adsorption of DR23: (a) XPS spectra of OB, (b) XPS spectra of OAOB, (c) C1s spectra of OB before and after adsorption of DR23, and (d) C1s spectra of OAOB before and after adsorption of DR23.

Table 7
FTIR peaks ascription of OB and OAOB before and after adsorption of DR23

OB		OAOB		Ascription
Before adsorption (cm^{-1})	After adsorption (cm^{-1})	Before adsorption (cm^{-1})	After adsorption (cm^{-1})	
479–797	476–797	463–797	464–797	Vibration of Si–O–Si
1,036	1,036	1,081	1,082	C–OH stretching
–	–	1,314; 1,420	1,315; 1,420	Calcium oxalate hydrates
–	1,385	–	1,385	C–NO_2 symmetric stretching
–	1,492	–	1,491	CH_3 asymmetric bending
–	1,535	–	1,536	C–N stretching
1,618	1,611	1,615	1,618	C=O stretching in carboxylic
–	–	1,666	1,660	COO^- antisymmetric stretching
–	–	3,342	–	O–H stretching
3,431	3,417	3,423	3,424	

Table 8
XPS data of OB and OAOB before and after adsorption of DR23

Element	OB		OB with DR23		Ascription
	BE (eV)	I_i (% at.)	BE (eV)	I_i (% at.)	
C1a	284.29	20.073	284.28	17.621	Non-functionalized carbon sp² atoms
C1b	284.80	26.580	284.76	27.210	Non-functionalized carbon sp³ atoms
C2a	285.38	27.455	285.32	27.114	C–O
C2b	286.40	19.168	286.24	19.168	C=O
C2c	289.06	6.724	288.92	8.886	COO–
Total C	–	37.02	–	42.26	
Total O	–	60.55	–	54.38	
Total N	–	2.43	–	3.36	
	OAOB		OAOB with DR23		
	BE (eV)	I_i (% at.)	BE (eV)	I_i (% at.)	
C1a	284.22	13.380	284.31	17.624	Non-functionalized carbon sp² atoms
C1b	284.73	20.012	284.81	24.577	Non-functionalized carbon sp³ atoms
C2a	285.28	18.479	285.38	23.803	C–O
C2b	286.20	11.766	286.38	16.657	C=O
C2c	289.22	36.361	289.30	17.342	COO–
Total C	–	34.28	–	60.90	
Total O	–	63.94	–	27.34	
Total N	–	1.79	–	11.76	

DR23 molecules. The peak area of component represented the percentage content of carbon atom in this component [41]. The two components (C1a+C1b), which were non-functionalized represented 46.65% and 33.392% of the total area of the C1s in OB and OAOB, respectively. The three components representing carbon atoms functionalized by oxygen atoms (C2a+C2b+C2c) took 53.35% and 66.61% of total area in OB and OAOB, respectively, and the most intensive was component C2a in OB and C2c in OAOB, indicating that, by modification, the percentage content of the active groups (C–O, C=O–, COO–) increased, and the C–O interacted with DR23 molecule as the main active group in OB, while in case of OAOB, the COO– as the main active group interacted with DR23 molecule. The total nitrogen content in OB and OAOB both increased after adsorption of DR23, showing that the DR23 had attached onto the two adsorbents. The above result verified the result of FTIR analysis.

3.4.3. Zeta potential characteristics before and after adsorption

Zeta potential reflects the potential on the surface of a particle, which is produced by the protonation and deprotonation of the surface functional groups [42]. The surface potential forms an electric double layer on the particle surface. The ion adsorbed by electrostatic interaction could not change the surface potential of the particle, because it is only in the diffusion layer, and the ion adsorbed by intermolecular interaction can enter the base of the electric double layer, which can change the surface potential of the particle [43,44]. As shown in Figs. 8a and b, when pH value was 3, the values of zeta potential of OB and OAOB were both positive, indicating OB and OAOB carried positive charges. As the pH value increases, the zeta potential became negative because of the ionization of surface functional groups, and the surface negative potentials increased with the increase of pH values. When the DR23 was adsorbed, the negative charge on the OB and OAOB surface became more and more, it is because that DR23 molecule also carries negative charge on the surface. The more DR23 was adsorbed, the more negative charge attached on the OB and OAOB, which verified that the OB and OAOB absorbed DR23 molecule by functional group interaction, leading DR23 molecule enter into the base of the electric double layer, and then changed the value of zeta potential.

3.5. Model fitting

3.5.1. Adsorption isotherms

The experimental isotherm process of DR23 onto OB and OAOB was simulated by well-known Freundlich, Langmuir, Dubinin–Radushkevich (D-R) and Temkin isotherm models. In Freundlich model, the surface heterogeneity and exponential distribution of the active sites and their energies were included, which can describe reversible adsorption but not be restricted to monolayer formation. For Langmuir model, a monolayer deposition on a surface with a finite number of identical sites was assumed, and it represented the chemisorption. D-R isotherm model generally used a Gaussian energy distribution onto a heterogeneous surface to explain the adsorption mechanism. And Temkin isotherm model was applied to express the interaction between adsorbate and adsorbent [45]. The equations of the four models are given as follows:
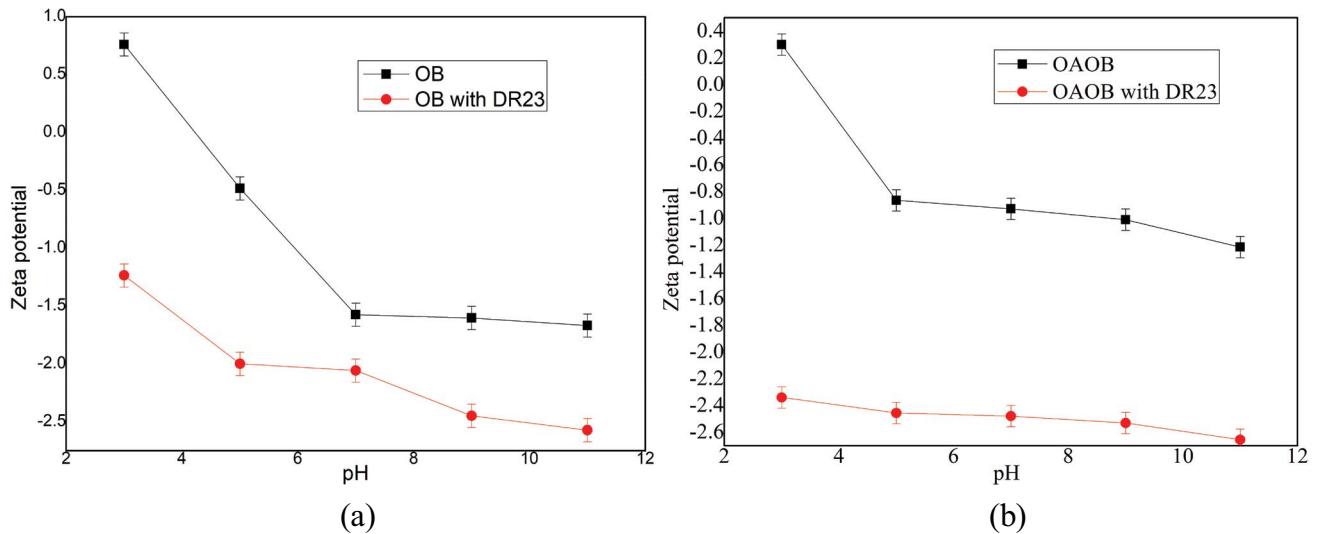
Fig. 8. Zeta potential variation before and after adsorption of DR23 on OB and OAOB, (a) OB and (b) OAOB.

Langmuir isotherm:

$$\frac{C_e}{q_e} = \frac{1}{K_L q_m} + \frac{C_e}{q_m} \tag{4}$$

Freundlich isotherm:

$$\ln q_e = \ln K_F + \frac{1}{n} \ln C_e \tag{5}$$

Temkin isotherm equation:

$$q_e = \frac{RT}{b_T} \ln k_T + \frac{RT}{b_T} \ln C_e \tag{6}$$

D-R adsorption isotherm equation:

$$\ln(q_e) = \ln(q_m) - \beta \varepsilon^2 \tag{7}$$

$$\varepsilon = RT \ln\left(1 + \frac{1}{C_e}\right) \tag{8}$$

$$E_a = \frac{1}{\sqrt{2\beta}} \tag{9}$$

where q_m (mg/g) is the maximum adsorption capacity of DR23, q_e (mg/g) and C_e (mg/L) are the adsorption capacity of DR23 and concentration of the DR23 solution at equilibrium, K_L (L/mg), n, K_F (L/mg), b_T, K_T (L/mg), β (mol²/kJ²), and ε are the constants in their own equations, R (8.314 J/mol K) is the gas constant, T (K) is the Fahrenheit temperature.

Fig. 9 shows the adsorption isotherms of DR23 onto OB and OAOB by above four models, and the fitting parameters are listed in Table 8. In Langmuir model, the adsorption data is plotted as C_e vs. C_e/q_e, the adsorption data of OB and OAOB were both in good agreement with the Langmuir isotherm model with R^2 0.973 and 0.992, respectively, which indicated the adsorption of DR23 onto

OB and OAOB fitted the monolayer sorption with finite identical adsorption sites on the homogeneous surface [46]. The maximum adsorption capacities of OB and OAOB for DR23 were 313.480 and 336.700 mg/g, respectively, calculated by the Langmuir equation. And the adsorption capacity increased after modified by OA.

The $R_L = 1/(1 + C_0 K_L)$ is a dimensionless constant factor, which can be used to judge the sorption process is "favorable" or "unfavorable" [47], where C_0 is the highest initial concentration of adsorbate. $R_L = 0$ implies the sorption is irreversible, R_L within 0 and 1 reveals the sorption is favorable, $R_L = 1$ means the sorption is linear, and R_L more than 1 reveals the sorption is unfavorable [47], the R_L values of OB and OAOB in this experiment were 0.395 and 0.426, respectively, both of which were between 0 and 1, indicating adsorption of the DR23 onto OB and OAOB were both favorable. In addition, increase of the initial concentration of DR23 enhanced the adsorption process. The order of the R_L value was OAOB > OB, showing the favorability of adsorption was OB > OAOB, while the adsorption capacity order was OAOB > OB, indicating the monolayer coverage sorption may not be the only adsorption mechanisms.

In Freundlich equation, the adsorption data are plotted as $\ln q_e$ vs. $\ln C_e$, should result in a straight line with slope "$1/n$", and intercept $\ln k_f$, the intercept and slope are indicators of adsorption capacity and adsorption intensity, respectively [46]. As shown in Table 9, the adsorption of DR23 onto OB and OAOB also fitted the Freundlich isotherm model well with R^2 0.977 and 0.966, respectively, revealing that the adsorption process also contained multi-layer adsorption onto heterogeneous surface. The value of "$1/n$" is usually applied to describe the favorability of multi-layer sorption process. $1/n$ less than 0.5 implies favorable sorption; $1/n$ more than 2 represents unfavorable sorption [48]. The $1/n$ values of OB and OAOB were 0.517, 0.571, respectively, both of which more than 0.5, indicating the multi-layer adsorption of DR23 onto OB and OAOB were not favorable.

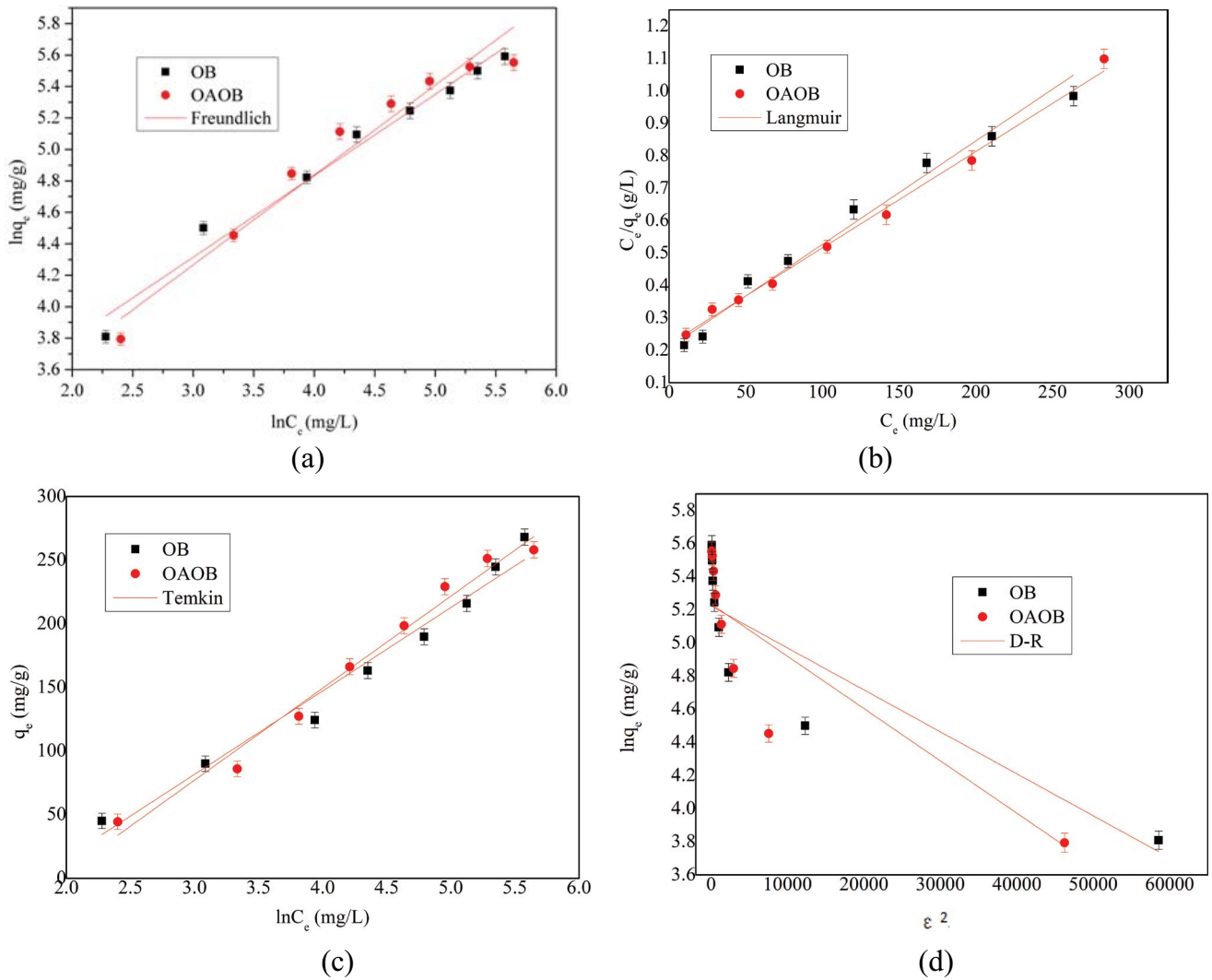The adsorption data were also simulated by the Temkin isotherm model. Unlike Freundlich and Langmuir

Fig. 9. Sorption isotherms of DR23 on the OB and OAOB: (a) Freundlich isotherm parameter, (b) Langmuir isotherm parameter, (c) Temkin isotherm parameter, and (d) D-R isotherm parameter (dosage, 0.1 g; temperature, 25°C; initial concentration, 100–800 mg/L; initial pH, 6.0–7.0).

Table 9
Isotherm parameters for the adsorption of DR23

Biochar samples	Langmuir				Freundlich	
	q_m (mg/g)	K_L (L/mg)	R^2	K_F (L/mg)	$1/n$	R^2
OB	313.480	0.0153	0.973	15.832	0.517	0.975
OAOB	336.700	0.0135	0.992	12.833	0.571	0.955

	Temkin			D-R			
	b_T	K_T (L/mg)	R^2	q_m (mg/g)	B (mol²/kJ²)	E_a (kJ/mol)	R^2
OB	37.817	0.173	0.972	185.646	2.53284E-05	198.699	0.802
OAOB	34.279	0.145	0.980	187.923	3.15734E-05	177.967	0.892

models, Temkin is assumed that the adsorption energy linearly decreases as the result of the surface coverage. The Temkin isotherm model simulated sorption process well with R^2 0.972 for OB, and 0.980 for OAOB, respectively, showing the binding energies on surface of OB and OAOB were uneven. The non-uniform distribution may be caused by the chemisorption process, especially the electrostatic adsorption [49]. Thereby, the electrostatic interaction might be a mechanism in the sorption of DR23 onto OB and OAOB, which was consistent with the result of the effect of pH analysis.

Fig. 9d shows the simulation of the D-R model, through Dubinin–Radushkevich isotherm, the physical adsorption or chemical adsorption can be judged by calculating the Gaussian energy distribution on a heterogeneous surface. This model is more suitable for the intermediate range of concentrations and high solute activities data. The E_a was used to express the type of adsorption, $1 < E_a < 8$ kJ/mol indicates that it is mainly the physical adsorption, $8 < E_a < 16$ kJ/mol indicates that the adsorption is ion exchange one, $E_a > 16$ kJ/mol reveals that it is considered to be chemical adsorption [49]. In this study, the E_a were 198.699 and 177.967 kJ/mol, respectively, both larger than 16 kJ/mol, illustrating the adsorption process may be mainly the chemisorption, while the regression coefficients of the OB and OAOB were 0.802 and 0.892, it did not fit the adsorption data well. In order to prove the results, the adsorption thermodynamics would be also discussed in the following paragraphs.

Table 10 lists the adsorption capacities of some adsorbents used in the previous literature for DR23, comparing with that of OB and OAOB in this study [9,32,50–53]. The results showed that the adsorption capacities of OB and OAOB were much higher than the other adsorbents reported in the previous articles, indicating the OB and OAOB can be an excellent adsorbent for the treatment of DR23-polluted wastewater.

3.5.2. Adsorption kinetics

In order to investigate the mechanisms of the DR23 adsorption process, the pseudo-first-order, pseudo-second-order, intraparticle diffusion, Elovich kinetic models were used to simulate the dynamic experimental data and detect the dynamic adsorption processes of the DR23 onto the OB and OAOB.

Pseudo-first-order kinetic equation:

$$\ln\left(q_e - q_t\right) = \ln q_e - k_1 t \tag{10}$$

Pseudo-second-order kinetic equation:

$$\frac{t}{q_t} = \frac{1}{k_2 q_e^2} + \frac{t}{q_e} \tag{11}$$

Intraparticle diffusion equations:

$$q_t = k_d t^{1/2} + C \tag{12}$$

Elovich equations:

$$q_t = \left(\frac{1}{\beta}\right)\ln(\alpha\beta) + \left(\frac{1}{\beta}\right)\ln(t) \tag{13}$$

Table 10
Comparison of various adsorbents investigated recently by means of DR23 adsorption capacity

Adsorbent	q_m (mg/g)	Ref.
MMWCNTs-Fe$_3$C	172.4	[9]
Orange peel	10.72	[50]
TiO$_2$	35.2	[51]
ZnO nanoparticles	43.66	[52]
Cationized sawdust	65.8	[53]
SRHB	59.77	[32]
OB	313.48	This study
OAOB	336.70	This study

where q_e (mg/g) and q_t (mg/g) are adsorption capacity at equilibrium and time t; k_1 (1/min), k_2 (g/m·min), and k_d (g/mg·min$^{1/2}$) are the rate constants in pseudo-first-order, pseudo-second-order and intraparticle diffusion model, respectively, C is a constant, α (mg/g min) is the initial adsorption coefficient, and β (g/mg) is the desorption coefficient.

Fig. 10 shows the simulated curves by the four kinetic models, and the fitting parameters are listed in Table 11. The results indicated that the theoretical $q_{e,cal}$ value of pseudo-first-order did not agree to the experimental $q_{e,exp}$ values at all concentrations studied with poor correlation coefficient. While the pseudo-second-order model fitted the adsorption process better than the other kinetic models, the correlation coefficients were 0.999 for OB, and 0.992 for OAOB, and the experimental values $q_{e,exp}$ approached to the theoretical values $q_{e,cal}$ [54], the pseudo-second-order model assumes that the chemical adsorption of the adsorbate onto adsorbent is a rate-limiting process [55], illustrating the adsorption of DR23 onto the surface of OB and OAOB might be chemisorption, and the adsorption process took a relatively long time to achieve equilibrium.

In general, surface diffusion and pore diffusion are two types of adsorption behaviors. For further verifying the dynamic adsorption process, the Elovich model and intraparticle model were also used to simulate the adsorption dynamic data. Fig. 10c shows that the intraparticle fitting plots of OB and OAOB were both multi-linear, illustrating there were two or more steps in the adsorption process. The first linear plot presented gradual adsorption stage, in this step intraparticle diffusion was rate-limiting [56]. The second linear plot was the equilibrium stage in which the intraparticle diffusion is further slowed down because of the decreasing of the concentration in the solution [55]. When the plot passes through the origin, the intraparticle diffusion is dominant; otherwise, it involves other forms of adsorption [12]. Fig. 10c shows that the plots of OB and OAOB both did not pass through the origin, suggesting that the external diffusion also affected and controlled the adsorption rate. The Elovich isotherm model reflects the heterogeneous diffusion and it is associated with the diffusion factor and reaction rate [2]. The Elovich model had a good correlation with R^2 0.95766 for OB, 0.93769 for OAOB, respectively, revealing that the heterogeneous diffusion may also be included in the adsorption of DR23 onto OB and OAOB.
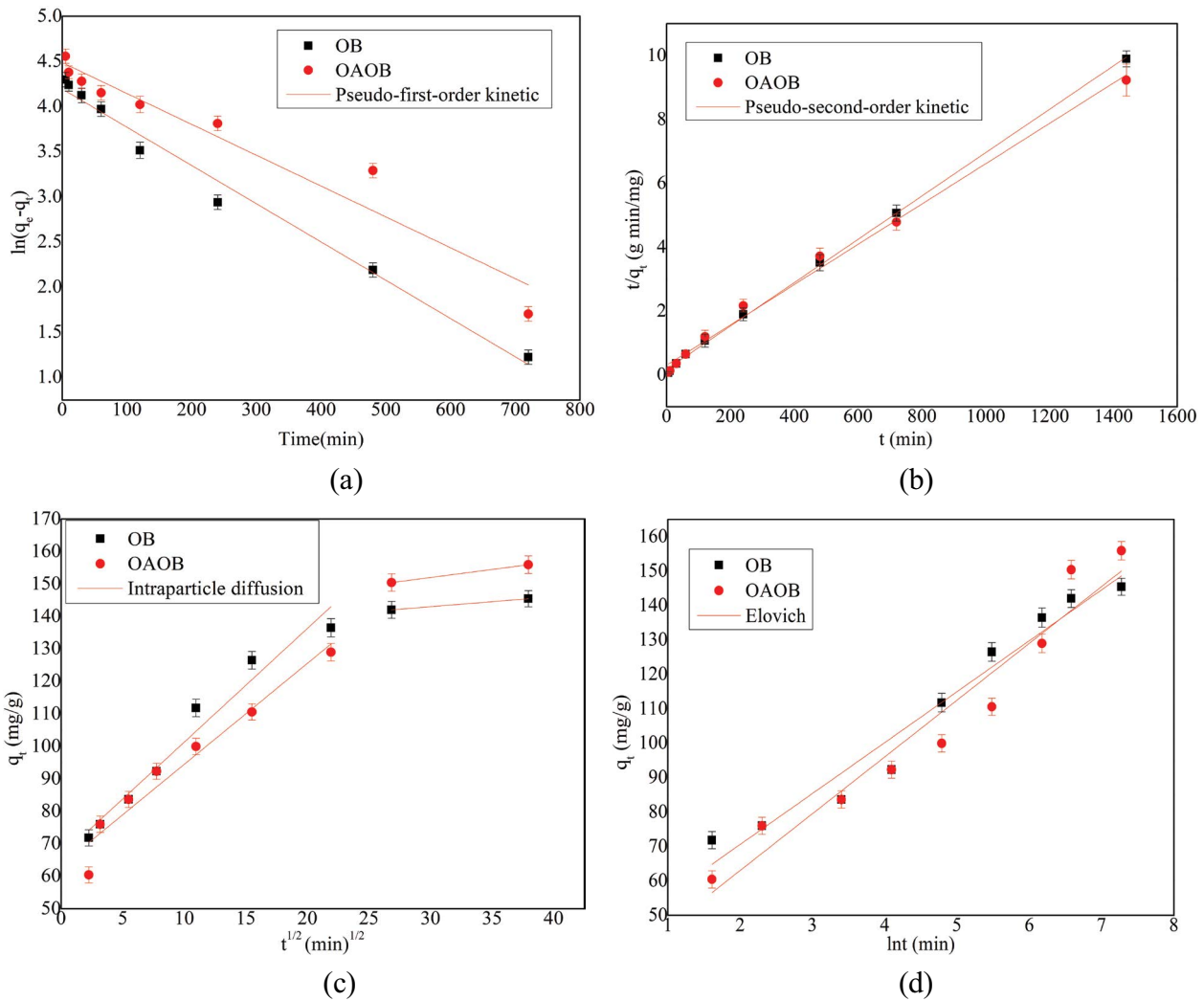
Fig. 10. Kinetic spectra for the sorption of DR23 on OB and OAOB: (a) pseudo-first-order model, (b) pseudo- second-order model, (c) intraparticle diffusion model, and (d) Elovich model (biochar dosage, 0.1 g; temperature, 25°C; t, 1,440 min; initial concentration, 400 mg/L; initial pH, 6.0–7.0).

3.5.3. Adsorption thermodynamics of DR23 by OB and OAOB

For confirming the main adsorption mechanism of the DR23 onto OB and OAOB, the adsorption thermodynamic was conducted, the thermodynamic behavior was described by the variation of free energy ($\Delta G°$, kJ/mol), entropy ($\Delta S°$, kJ/mol K) and enthalpy ($\Delta H°$, kJ/mol). They were calculated by Eqs. (14)–(16) as follows:

$$\Delta G° = -RT \ln\left(K_e^0\right) \tag{14}$$

$$\ln\left(K_e^0\right) = \frac{\Delta S°}{R} - \frac{\Delta H°}{RT} \tag{15}$$

$$K_e^0 = \frac{\left(1{,}000 \cdot K_g \cdot \text{molecular weight of adsorbate} \times [\text{adsorbate}]^0\right)}{\gamma} \tag{16}$$

where T is the Kelvin temperature (K), R is the gas constant (8.314 J/mol K), K_e^0 is calculated by Eq. (16) [57], γ is the activity coefficient, $[\text{adsorbate}]^0$ is the standard concentration (1 mol/L), K_g is the K of the best fitted isotherm model. $\Delta G°$ was obtained by Eq. (14), and the $\Delta H°$ and $\Delta S°$ can be obtained by plotting the $\ln K_e^0$ vs. $1/T$ as Fig. 11.

Table 12 lists the thermodynamic parameters of the DR23 on OB and OAOB. The $\Delta G°$ of DR23 was negative, illustrating that the sorption of DR23 on OB and OAOB was spontaneous. OB and OAOB both had the positive $\Delta H°$, indicating that the DR23 sorption onto OB and OAOB was endothermic [45]. The $\Delta S°$ of OB and OAOB for DR23 was positive, suggesting the randomness at the interface of the two biochar increased during the adsorption process [8], enhancement of adsorption capacity of DR23 onto OB and OAOB at higher temperature may be attributed to the enlargement of pore size or activation of the adsorbent surface [45].

When the ΔH^0 within 2.1–20.9 kJ/mol, it is mainly the physical adsorption, and the binding energy might be

Table 11
Kinetic parameters for the adsorption of DR23 on OB and OAOB

| Kinetic models	Samples	
	OB	OAOB
$q_{e,exp}$ (mg/g)	145.443	155.919
Pseudo-first-order		
$q_{e,cal}$ (mg/g)	66.382	88.881
k_1 (min^{-1})	0.00424	0.00342
R^2	0.984	0.928
Pseudo-second-order		
$q_{e,cal}$ (mg/g)	147.275	158.479
k_2 (g/mg min)	0.000262	0.000131
R^2	0.999	0.993
Particle		
$K_{d,1}$ (mg/g min$^{1/2}$)	3.501	3.108
C_1	66.308	63.414
R^2	0.956	0.940
$K_{d,2}$ (mg/g min$^{1/2}$)	0.307	0.495
C_2	133.810	137.141
R^2	1	1
Elovich		
α	236.587	101.893
β	0.0676	0.061
R^2	0.958	0.938
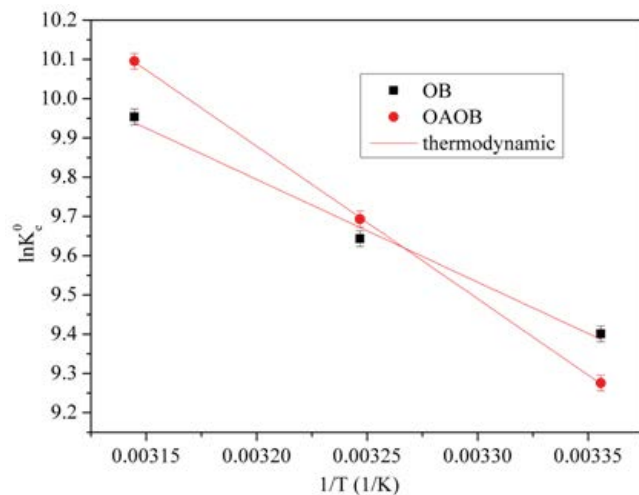
Fig. 11. Plot of ln$K$ and $1/T$: 0.1 g, temperature: 289 K, 308 K, 318 K; t: 1,440 min; initial concentration: 100–800 mg/L; initial pH: 6.0–7.0.

the electrostatic interaction or Van der Waals' force, when the $\Delta H°$ within 20.9–418.4 kJ/mol, the chemisorption is the main mechanism. The $\Delta H°$ values of the DR23 onto OB and OAOB were both within the 20.9–418.4 kJ/mol. So the adsorption of DR23 onto OB and OAOB was both

mainly chemisorption, it agreed with the result of the D-R isotherm model.

3.6. Adsorption mechanisms

The adsorption mechanisms of the DR23 onto OB and OAOB were complex. The physical properties showed that the OB and OAOB both had large BET area, total pore volume, and average pore diameters were 1.7–3 times larger than DR23 molecule sizes. These characteristics enabled OB and OAOB have good physical adsorption properties towards DR23, and the surface was covered with a large amount of SiO_2, which also offered adsorption sites for DR23. Therefore, the physical adsorption of OB and OAOB included pore diffusion, surface participation, and surface mineral constituent's adsorbing.

The result of zeta potential analysis indicated that there were surface functional group interaction in the adsorption process, and the FTIR and XPS results proved it, which showed the –OH, –COOH on the surface of OB, the –OH, –COOH, –COOR on the surface of OAOB interacted with the functional groups of DR23 molecule. Because of the aromatic structure, the OB and OAOB might also formed π–π stacking interaction with DR23. The analysis of pH effect as shown in Fig. 5a indicated the electrostatic interaction accounted for a certain proportion in the adsorption process.

Adsorption kinetics verified the adsorption of the DR23 on OB and OAOB was rate-limited, and the process contained two stages, stage one expressed gradual adsorption of DR23, the stage two expressed that sorption rate gradually fell down and then reached stable because of the concentration decreasing of DR23 solution. The adsorption isotherm showed that mono-layer coverage and multilayer coverage both took place, the mono-layer adsorption of the DR23 was favorable, while the multilayer coverage adsorption was not favorable. Temkin model verified the electrostatic interaction accounted for a large proportion in the adsorption process, which agreed with the result of pH influence analysis. The values of E_a and $\Delta H°$ implied the main adsorption mechanism of the DR23 onto OB and OAOB were chemisorption. Fig. 12 shows the adsorption mechanism of DR23 onto OB and OAOB.

4. Conclusion

The sludge-rice husk biochar (with ratio 7:3) has been proven having excellent adsorption characteristics for removal of Direct Red 23 (DR23) from wastewater. RSM statistical analysis revealed that the optimum conditions of biochar preparation for the highest adsorption of DR23 were recorded to have temperature of 651.444°C, heating rate of 10°C/min, and residence time of 4.683 h. OB and OAOB emerged as better promising adsorbents in the adsorption of DR23 with adsorption capacity 313.48 and 336.70 mg/g, respectively. Freundlich, Langmuir and Temkin models all matched the experimental data well, and the adsorption kinetic obeyed pseudo-second-order model. The thermodynamic study implied that adsorption of DR23 onto OB and OAOB was spontaneous and

Table 12
Thermodynamic parameters for the adsorption of the DR23

	Temperature (K)	q_m (mg/g)	K_L (L/mg)	K_e^0	$\Delta G°$ (kJ/mol)	$\Delta H°$ (kJ/mol)	$\Delta S°$ (J/mol K)
	298	313.480	0.0153	12,097.56	−23.291		
OB	308	314.620	0.0195	13,046.39	−24.693	21.750	151.030
	318	317.765	0.0266	13,916.14	−26.316		
	298	336.700	0.0135	10,674.32	−22.981		
OAOB	308	339.235	0.0205	16,208.44	−25. 627	32.311	185.526
	318	344.176	0.0307	24,243.94	−25. 852		
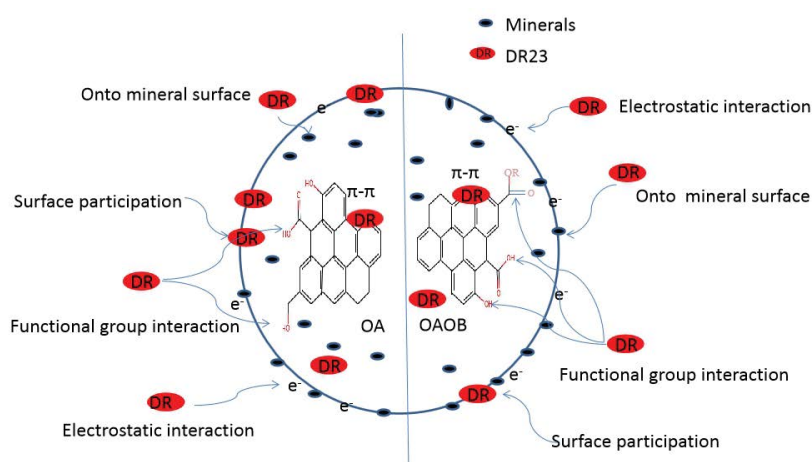
Fig. 12. Adsorption mechanism diagram of DR23 onto OB and OAOB.

endothermic. Hence, sludge-rice husk biochar is a potential candidate for dye-polluted wastewater treatment.

References

[1] J.W. Jin, Y.N. Li, J.Y. Zhang, S.C. Wu, Y.C. Cao, P. Liang, J. Zhang, M.H. Wong, M.Y. Wang, S.D. Shan, P. Christie, Influence of pyrolysis temperature on properties and environmental safety of heavy metals in biochars derived from municipal sewage sludge, J. Hazard. Mater., 320 (2016) 417–426.
[2] L. Tang, J.F. Yu, Y. Pang, G.M. Zeng, Y.C. Deng, J.J. Wang, X.Y. Ren, S.J. Ye, B. Peng, H.P. Feng, Sustainable efficient adsorbent: Alkali-acid modified magnetic biochar derived from sewage sludge for aqueous organic contaminant removal, Chem. Eng. J., 336 (2017) 160–169.
[3] H.L. Lu, W.H. Zhang, Y.X. Yang, X.F. Huang, S.Z. Wang, R.L. Qiu, Relative distribution of Pb²⁺ sorption mechanisms by sludge-derived biochar, Water Res., 46 (2012) 854–862.
[4] M.K. Hossain, V. Strezov, K.Y. Chan, A. Ziolkowski, P.F. Nelson, Influence of pyrolysis temperature on production and

nutrient properties of wastewater sludge biochar, J. Environ. Manage., 92 (2011) 223–228.
[5] T. Chen, Y.X. Zhang, H.T. Wang, W.J. Lu, Z.Y. Zhou, Y.C. Zhang, L.L. Ren, Influence of pyrolysis temperature on characteristics and heavy metal adsorptive performance of biochar derived from municipal sewage sludge, Bioresour. Technol., 164 (2014) 47–54.
[6] A. Mendez, A. Gomez, J. Paz-Ferreiro, G. Gasco, Effects of sewage sludge biochar on plant metal availability after application to a Mediterranean soil, Chemosphere, 89 (2012) 1354–1359.
[7] J. Ifthikar, J. Wang, Q. Wang, T. Wang, H. Wang, A. Khan, A. Jawad, T. Sun, X. Jiao, Z. Chen, Highly efficient lead distribution by magnetic sewage sludge biochar: sorption mechanisms and bench applications, Bioresour. Technol., 238 (2017) 399–406.
[8] A.A. Atia, A.M. Donia, W.A. Al-Amrani, Adsorption/desorption behavior of acid orange 10 on magnetic silica modified with amine groups, Chem. Eng. J., 150 (2009) 55–62.
[9] W. Konicki, I.P. Ech, E. Mijowska, I. Jasińska, Adsorption of anionic dye Direct Red 23 onto magnetic multi-walled carbon nanotubes-Fe3C nanocomposite: kinetics, equilibrium and thermodynamics, Chem. Eng. J., 210 (2012) 87–95.
[10] R. Kamaraj, A. Pandiarajan, S. Vasudevan, S. Vasudevan, Facial one-pot electrosynthesis of zinc hydroxide for the adsorption of hazardous 2-(2-methyl-4-chlorophenoxy) propionic acid (MCPP) from water and its modelling studies, J. Environ. Chem. Eng., 6 (2018) 2017–2026.
[11] D.K. Mahmoud, M.A.M. Salleh, A.W.A.K. Wan, A. Idris, Z.Z. Abidin, Batch adsorption of basic dye using acid treated kenaf fibre char: equilibrium, kinetic and thermodynamic studies, Chem. Eng. J., 181–182 (2012) 449–457.
[12] B.H. Hameed, D.K. Mahmoud, A.L. Ahmad, Equilibrium modeling and kinetic studies on the adsorption of basic dye

by a low-cost adsorbent: coconut (*Cocos nucifera*) bunch waste, J. Hazard. Mater., 158 (2008) 65–72.

[13] Y.F. Feng, D.D. Dionysiou, Y.H. Wu, H. Zhou, L.H. Xue, S.Y. He, L.Z. Yang, Adsorption of dyestuff from aqueous solutions through oxalic acid-modified swede rape straw: adsorption process and disposal methodology of depleted bioadsorbents, Bioresour. Technol., 138 (2013) 191–197.

[14] A. Kausar, M. Iqbal, A. Javed, K. Aftab, Z. Nazli, H.N. Bhatti, S. Nouren, Dyes adsorption using clay and modified clay: a review, J. Mol. Liq., 256 (2018) 395–407.

[15] X.J. Tong, J.Y. Li, J.H. Yuan, R.K. Xu, Adsorption of Cu(II) by biochars generated from three crop straws, Chem. Eng. J., 172 (2011) 828–834.

[16] W.S.W. Ngah, L.C. Teong, M.A.K.M. Hanafiah, Adsorption of dyes and heavy metal ions by chitosan composites: a review, Carbohydr. Polym., 83 (2011) 1446–1456.

[17] P. Ganesan, R. Kamaraj, S. Vasudevan, Application of isotherm, kinetic and thermodynamic, models for the adsorption of nitrate ions on graphene from aqueous solution, J. Taiwan Inst. Chem. Eng., 44 (2013) 808–814.

[18] R. Kamaraj, S. Vasudevan, Decontamination of selenate from aqueous solution by oxidized multi-walled carbon nanotubed, Powder Technol., 274 (2015) 268–275.

[19] A. Enders, K. Hanley, T. Whitman, S. Joseph, J. Lehmann, Characterization of biochars to evaluate recalcitrance and agronomic performance, Bioresour. Technol., 114 (2012) 644–653.

[20] A. Freddo, C. Cai, B.J. Reid, Environmental contextualisation of potential toxic elements and polycyclic aromatic hydrocarbons in biochar, Environ. Pollut., 171 (2012) 18–24.

[21] X.J. Zuo, Z.G. Liu, M.D. Chen, Effect of H_2O_2 concentrations on copper removal using the modified hydrothermal biochar, Bioresour. Technol., 207 (2016) 262–267.

[22] G.X. Yang, H. Jiang, Amino modification of biochar for enhanced adsorption of copper ions from synthetic wastewater, Water Res., 48 (2014) 396–405.

[23] F. Güzel, H. Sayğili, G.A. Sayğılı, F. Koyuncu, C. Yılmaz, Optimal oxidation with nitric acid of biochar derived from pyrolysis of weeds and its application in removal of hazardous dye Methylene blue from aqueous solution, J. Cleaner Prod., 144 (2017) 260–265.

[24] B.L. Chen, Z.M. Chen, S.F. Lv, A novel magnetic biochar efficiently sorbs organic pollutants and phosphate, Bioresour. Technol., 102 (2011) 716–723.

[25] J. Jiang, R.K. Xu, T.Y. Jiang, Z. Li, Immobilization of Cu(II), Pb(II) and Cd(II) by the addition of rice straw derived biochar to a simulated polluted Ultisol, J. Hazard. Mater., 229–230 (2012) 145–150.

[26] N. Liu, A.B. Charrua, C.H. Weng, X.L. Yuan, F. Ding, Characterization of biochars derived from agriculture wastes and their adsorptive removal of atrazine from aqueous solution: a comparative study, Bioresour. Technol., 198 (2015) 55–62.

[27] A. Navya, S. Nandhini, S. Sivamani, N. Sivarajasekar, A. Hosseini-Bandegharaei, Preparation and characterization of cassava stem biochar for mixed reactive dyes removal from simulated effluent, Desal. Water Treat., 189 (2020) 440–451.

[28] E. Kaçan, Optimum BET surface areas for activated carbon produced from textile sewage sludges and its application as dye removal, J. Environ. Manage., 166 (2015) 116–123.

[29] A.F.M. Streit, L.N. Côrtes, S.P. Druzian, M. Godinho, G.C. Collazzo, D. Perondi, G.L. Dotto, Development of high quality activated carbon from biological sludge and its application for dyes removal from aqueous solutions, Sci. Total Environ., 660 (2019) 277–287.

[30] W.S. Chen, Y.P. Guo, X. Mi, Y. Yu, G.T. Li, Enhanced adsorptive removal of methylene blue by low-temperature biochar derived from municipal, Desal. Water Treat., 188 (2020) 257–265.

[31] T. Wang, Y.C. Chen, J.P. Li, Y.J. Xue, J.X. Liu, M. Mei, H.B. Hou, S. Chen, Co-pyrolysis behavior of sewage sludge and rice husk by TG-MS and residue analysis, J. Cleaner Prod., 250 (2020) 119557.

[32] S. Chen, C.X. Qin, T. Wang, F.Y. Chen, X.L. Li, H.B. Hou, M. Zhou, Study on the adsorption of dyestuffs with different properties by sludge-rice husk biochar: adsorption capacity, isotherm, kinetic, thermodynamics and mechanism, J. Mol. Liq., 285 (2019) 62–74.

[33] R.S. Yuan, J.T. Zheng, R.B. Guan, Y.H. Liu, Immobilization of TiO_2 on microporous activated carbon fibers and their photodegradation performance for phenol, New Carbon Mater., 20 (2005) 45–50.

[34] A. Verganelaki, V. Kilikoglou, I. Karatasios, P. Maravelaki-Kalaitzaki, A biomimetic approach to strengthen and protect construction materials with a novel calcium-oxalate–silica nanocomposite, Construct. Build Mater., 62 (2014) 8–17.

[35] H.R. Yuan, T. Lu, H.Y. Huang, D.D. Zhao, N. Kobayashi, Y. Chen, Influence of pyrolysis temperature on physical and chemical properties of biochar made from sewage sludge, J. Anal. Appl. Pyrolysis., 112 (2015) 284–289.

[36] M.E. Mahmoud, G.M. Nabil, N.M. El-Mallah, H.I. Bassiouny, S. Kumar, T.M. Abdel-Fattah, Kinetics, isotherm, and thermodynamic studies of the adsorption of reactive red 195 A dye from water by modified Switchgrass Biochar adsorbent, J. Ind. Eng. Chem., 37 (2016) 156–167.

[37] T. Chen, Z.Y. Zhou, R. Han, R.H. Meng, H.T. Wang, W.J. Lu, Adsorption of cadmium by biochar derived from municipal sewage sludge: impact factors and adsorption mechanism, Chemosphere, 134 (2015) 286–293.

[38] R.K. Xu, S.C. Xiao, J.H. Yuan, A.Z. Zhao, Adsorption of methyl violet from aqueous solutions by the biochars derived from crop residues, Bioresour. Technol., 102 (2011) 10293–10298.

[39] Z.J. Fan, W. Kai, J. Yan, T. Wei, L.J. Zhi, J. Feng, Y.M. Ren, L.P. Song, F. Wei, Facile synthesis of graphene nanosheets via Fe reduction of exfoliated graphite oxide, ACS Nano, 5 (2011) 191–198.

[40] J.M. Simmons, B.M. Nichols, S.E. Baker, M.S. Marcus, O.M. Castellini, C.S. Lee, R.J. Hamers, M.A. Eriksson, Effect of ozone oxidation on single-walled carbon nanotubes, J. Phys. Chem. B, 110 (2006) 7113–7118.

[41] W. Konicki, M. Aleksandrzak, D. Moszyński, E. Mijowska, Adsorption of anionic azo-dyes from aqueous solutions onto graphene oxide: equilibrium, kinetic and thermodynamic studies, J. Colloid Interface Sci., 496 (2017) 188–200.

[42] Y. Zhou, L. Zhang, Z.J. Cheng, Removal of organic pollutants from aqueous solution using agricultural wastes: a review, J. Mol. Liq., 212 (2015) 739–762.

[43] H. Valdés, M. Sánchez-Polo, J. Rivera-Utrilla, C.A. Zaror, Effect of ozone treatment on surface properties of activated carbon, Langmuir, 18 (2002) 2111–2116.

[44] J. Park, Y.S. Ok, S. Kim, J. Cho, J. Heo, R.D. Delaune, D. Seo, Competitive adsorption of heavy metals onto sesame straw biochar in aqueous solutions, Chemosphere, 142 (2016) 77–83.

[45] R. Kamaraj, A. Pandiarajan, S. Jayakiruba, M. Naushad, S. Vasudevan, Kinetics, thermodynamics and isotherm modeling for removal of nitrate from liquids by facile one-pot emectrosynthesized nano zinc hydroxide, J. Mol. Liq., 215 (2016) 204–211.

[46] S. Vasudevan, J. Lakshmi, G. Sozhan, Simultaneous removal of Co, Cu, and Cr from water by electrocoagulation, Toxicol. Environ. Chem., 94 (2012) 1930–1940.

[47] G. Crini, P.M. Badot, Application of chitosan, a natural aminopolysaccharide, for dye removal from aqueous solutions by adsorption processes using batch studies: a review of recent literature, Prog. Polym. Sci., 33 (2008) 399–447.

[48] L.H. Liu, Y. Lin, Y.Y. Liu, H. Zhu, Q. He, Removal of Methylene Blue from aqueous solutions by sewage sludge based granular activated carbon: adsorption equilibrium, kinetics, and thermodynamics, J. Chem. Eng. Data, 58 (2013) 2248–2253.

[49] M. Kousha, E. Daneshvar, M.S. Sohrabi, M. Jokar, A. Bhatnagar, Adsorption of acid orange II dye by raw and chemically modified brown macroalga *Stoechospermum marginatum*, Chem. Eng. J., 192 (2012) 67–76

[50] S.S. Tahir, N. Rauf, Removal of a cationic dye from aqueous solutions by adsorption onto bentonite clay, Chemosphere, 63 (2006) 1842–1848.

[51] M. Arami, N.Y. Limaee, N.M. Mahmoodi, N.S. Tabrizi, Removal of dyes from colored textile wastewater by orange peel

adsorbent: equilibrium and kinetic studies, J. Colloid Interface Sci., 288 (2005) 371–376.

[52] S.S. Vieira, Z.M. Magriotis, N.A.V. Santos, M.D.G.A. Cardoso, A.A. Saczk, Macauba palm (*Acrocomia aculeata*) cake from biodiesel processing: an efficient and low cost substrate for the adsorption of dyes, Chem. Eng. J., 183 (2012) 152–161.

[53] X.L. Han, X.N. Niu, X.J. Ma, Adsorption characteristics of methylene blue on poplar leaf in batch mode: equilibrium, kinetics and thermodynamics, Korean J. Chem. Eng., 29 (2012) 494–502.

[54] R. Kamaraj, S. Vasudevan, Facile one-pot synthesis of nano-zinc hydroxide by electro-dissolution of zinc as a sacrificial anode and the application for adsorption of Th^{4+}, U^{4+}, and Ce^{4+} from aqueous solution, Res. Chem. Interned., 42 (2016) 4077–4095.

[55] M. Li, Q. Liu, L.J. Guo, Y.P. Zhang, Z.J. Lou, Y. Wang, G.R. Qian, Cu (II) removal from aqueous solution by *Spartina alterniflora* derived biochar, Bioresour. Technol., 141 (2013) 83–88.

[56] J.P. Chen, S. Wu, K.H. Chong, Surface modification of a granular activated carbon by citric acid for enhancement of copper adsorption, Carbon, 41 (2003) 1979–1986.

[57] E.C. Lima, A. Hosseini-Bandegharaei, J.C. Moreno-Piraján, I. Anastopoulos, A critical review of the estimation of the thermodynamic parameters on adsorption equilibria. Wrong use of equilibrium constant in the Van't Hoof equation for calculation of thermodynamic parameters of adsorption, J. Mol. Liq., 273 (2019) 425–434.